Formation of the methyl cation by photochemistry in a protoplanetary disk

Berné, O.; Martin-Drumel, M.-A.; Schroetter, I.; Goicoechea, J.R.; Jacovella, U.; Gans, B.; ... ; Wolfire, M.G.

Article

Formation of the methyl cation by photochemistry in a protoplanetary disk

https://doi.org/10.1038/s41586-023-06307-x

Received: 14 March 2023

Accepted: 9 June 2023

Published online: 26 June 2023

Check for updates

Olivier Berné[1]✉, Marie-Aline Martin-Drumel[2], Ilane Schroetter[1], Javier R. Goicoechea[3], Ugo Jacovella[2], Bérenger Gans[2], Emmanuel Dartois[2], Laurent H. Coudert[2], Edwin Bergin[4], Felipe Alarcon[4], Jan Cami[5,6,7], Evelyne Roueff[8], John H. Black[9], Oskar Asvany[10], Emilie Habart[11], Els Peeters[5,6,7], Amelie Canin[1], Boris Trahin[11], Christine Joblin[1], Stephan Schlemmer[10], Sven Thorwirth[10], Jose Cernicharo[3], Maryvonne Gerin[8], Alexander Tielens[12,13], Marion Zannese[11], Alain Abergel[11], Jeronimo Bernard-Salas[14,15], Christiaan Boersma[16], Emeric Bron[8], Ryan Chown[5,6], Sara Cuadrado[3], Daniel Dicken[11], Meriem Elyajouri[11], Asunción Fuente[17], Karl D. Gordon[18], Lina Issa[1], Olga Kannavou[11], Baria Khan[5], Ozan Lacinbala[19], David Languignon[8], Romane Le Gal[20,21], Alexandros Maragkoudakis[16], Raphael Meshaka[8], Yoko Okada[10], Takashi Onaka[22,23], Sofia Pasquini[5], Marc W. Pound[13], Massimo Robberto[18], Markus Röllig[24,25], Bethany Schefter[5], Thiébaut Schirmer[9,11], Ameek Sidhu[5,6], Benoit Tabone[11], Dries Van De Putte[18], Sílvia Vicente[26] & Mark G. Wolfire[13]

Forty years ago, it was proposed that gas-phase organic chemistry in the interstellar medium can be initiated by the methyl cation CH_3^+ (refs. 1–3), but so far it has not been observed outside the Solar System[4,5]. Alternative routes involving processes on grain surfaces have been invoked[6,7]. Here we report James Webb Space Telescope observations of CH_3^+ in a protoplanetary disk in the Orion star-forming region. We find that gas-phase organic chemistry is activated by ultraviolet irradiation.

As part of the PDRs4All Early Release Science programme on the James Webb Space Telescope (JWST) (pdrs4all.org)[8], we have obtained observations of the protoplanetary disk d203-506 (ref. 9). This object is situated in the Orion Bar, at about 0.25 pc from the massive, strongly ultraviolet (UV) emitting Trapezium stars that are at 414 pc from Earth[10], inside the Orion Nebula. The disk is about 100 astronomical units (AU) in radius, and has an estimated mass of roughly 10 M_J (O. Berné et al., manuscript in preparation). The central star of d203-506 has an estimated mass of $M_\star = 0.2 \pm 0.1\,M_\odot$ (O. Berné et al., manuscript in preparation), typical for stars of the Orion Nebula Cluster[11]. This star is obscured by the flared disk that is seen nearly edge-on[9]. Figure 1 shows integrated intensity images of the d203-506 disk (see Methods for details on JWST data reduction). This includes the emission of vibrationally and rotationally excited H_2 and CH^+, and fine-structure emission of oxygen ([O I]) and ionized iron ([Fe II]). The molecular emission arises from a hot (gas temperature T_{gas} of roughly 1,000 K) and dense (gas density $n_H > 10^5$ cm^{-3}) wind that is produced by photo-evaporation from the disk because of irradiation by far-UV photons (FUV, that is, photons with energies E in the range 6–13.6 eV) from the Trapezium stars (O. Berné et al., manuscript in preparation). The [Fe II] image shows the emission associated with a collimated jet. Some of the wind emission is cospatial with this jet, but overall the wind is more extended and creates a 'halo' around the disk.

The mid-infrared spectrum of d203-506 was obtained using the Mid-Infrared Instrument (MIRI)-Medium Resolution Spectroscopy (MRS) spectrometer onboard the JWST (see Methods for details) and is shown in Fig. 2. In the spectrum, we detect pure rotational lines of H_2 [0-0 S(1) to 0-0 S(8)] from which we derive an excitation temperature $T_{ex} = 923 \pm 48$ K (Methods). The straight line observed in the excitation diagram derived from these transitions (Extended Data Fig. 3) indicates that the excitation temperature of H_2 is close to the gas kinetic temperature, and thus confirms the presence of hot molecular gas in the wind of d203-506.

In addition to identified H_2 and H I emission lines (Methods), a strong residual emission consisting of a series of lines in the 6.5–8.0 μm range is observed (Fig. 2). This emission, as seen in the lower middle panel of Fig. 1, is spatially resolved and only present in d203-506. It is cospatial with H_2 and CH^+ emissions, with the best spatial correlation observed with the 2.12 μm line of vibrationally excited H_2 (Fig. 1). We conclude that the observed features in Fig. 2 are an astrophysical signal associated with emission from the wind of the d203-506 protoplanetary disk. We note, however, given that the angular resolution of MIRI is at the

[1]Institut de Recherche en Astrophysique et Planétologie, Université de Toulouse, CNRS, CNES, UPS, Toulouse, France. [2]Institut des Sciences Moléculaires d'Orsay, Université Paris-Saclay, CNRS, Orsay, France. [3]Instituto de Física Fundamental (CSIC), Madrid, Spain. [4]Department of Astronomy, University of Michigan, Ann Arbor, MI, USA. [5]Department of Physics and Astronomy, The University of Western Ontario, London, Ontario, Canada. [6]Institute for Earth and Space Exploration, The University of Western Ontario, London, Ontario, Canada. [7]Carl Sagan Center, SETI Institute, Mountain View, CA, USA. [8]LERMA, Observatoire de Paris, PSL University, Sorbonne Université, CNRS, Meudon, France. [9]Department of Space, Earth, and Environment, Chalmers University of Technology, Onsala Space Observatory, Onsala, Sweden. [10]I. Physikalisches Institut, Universität zu Köln, Cologne, Germany. [11]Institut d'Astrophysique Spatiale, Université Paris-Saclay CNRS, Orsay, France. [12]Leiden Observatory, Leiden University, Leiden, the Netherlands. [13]Astronomy Department, University of Maryland, College Park, MD, USA. [14]ACRI-ST, Centre dEtudes et de Recherche de Grasse (CERGA), Grasse, France. [15]INCLASS Common Laboratory, Grasse, France. [16]NASA Ames Research Center, Moffett Field, CA, USA. [17]Observatorio Astronómico Nacional (OAN,IGN), Madrid, Spain. [18]Space Telescope Science Institute, Baltimore, MD, USA. [19]KU Leuven Quantum Solid State Physics (QSP), Leuven, Belgium. [20]Institut de Planétologie et d'Astrophysique de Grenoble, Université Grenoble Alpes, CNRS, Grenoble, France. [21]Institut de Radioastronomie Millimétrique (IRAM), Saint-Martin d'Hères, France. [22]Department of Physics, Faculty of Science and Engineering, Meisei University, Tokyo, Japan. [23]Department of Astronomy, Graduate School of Science, The University of Tokyo, Tokyo, Japan. [24]Physikalischer Verein-Gesellschaft für Bildung und Wissenschaft, Frankfurt, Germany. [25]Physikalisches Institut, Goethe-Universität, Frankfurt, Germany. [26]Instituto de Astrofísica e Ciências do Espaço, Lisbon, Portugal. ✉e-mail: olivier.berne@irap.omp.eu

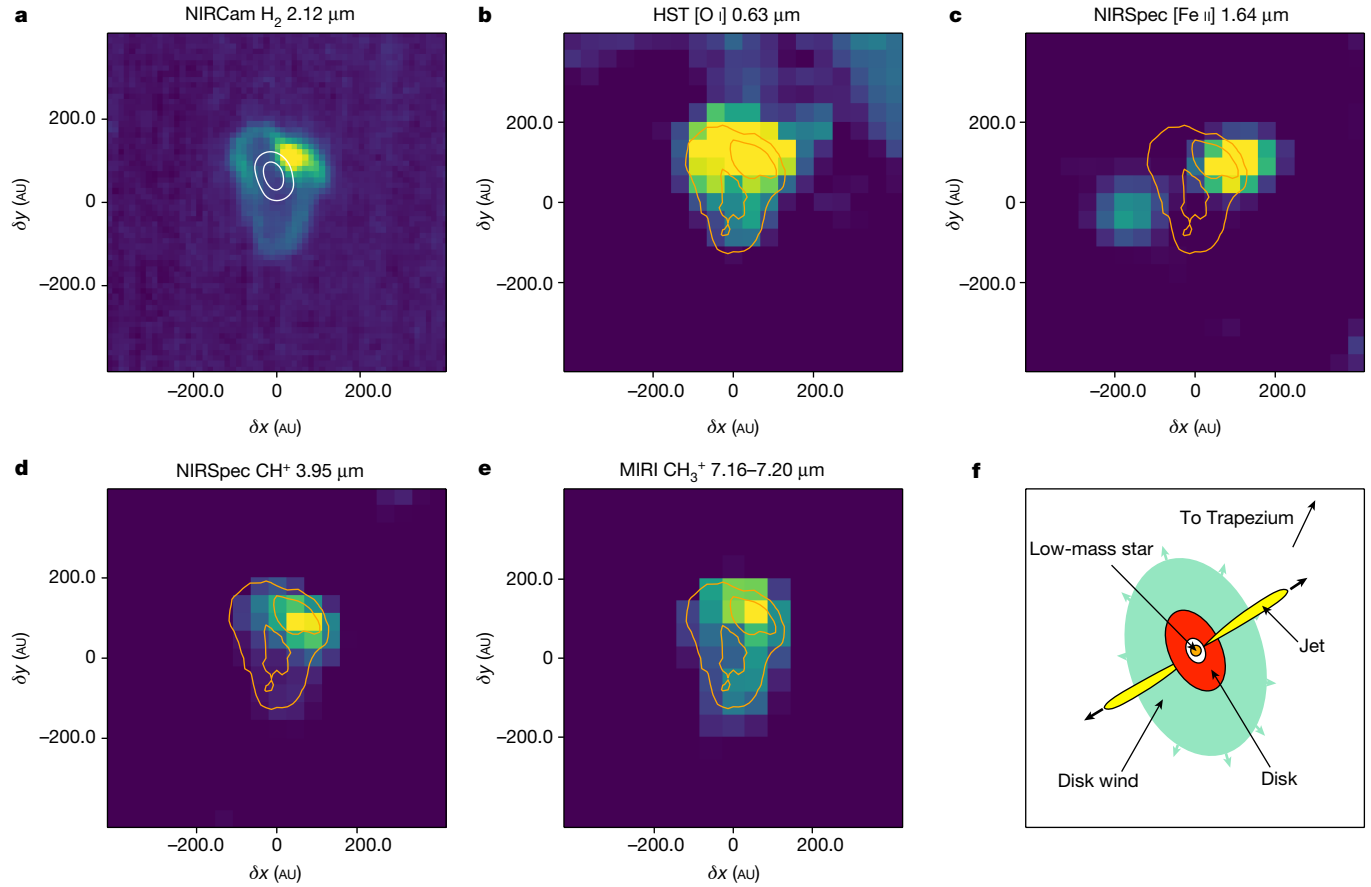

Fig. 1 | Overview of the d203-506 externally irradiated protoplanetary disk. **a**–**e**, Integrated intensity images from the JWST-NIRCam F212N filter (**a**), Hubble Space Telescope (HST) [O I] (**b**), JWST-NIRSpec [Fe II] (**c**), JWST-NIRSpec CH^+ 1–0 $P(7)$ at 3.95 μm (**d**) and JWST-MIRI-MRS integrated from 7.16 to 7.20 μm assigned to CH_3^+ (**e**). Each panel is centred at $\alpha = 05\,h\,35\,min\,20.318\,s$ and $\delta = -5°\,25'\,05.662''$, and all are 2″ × 2″ wide. Contours of NIRCam vibrationally excited H_2 (2.12 μm band) are represented in orange, and Atacama Large Millimeter/submillimeter Array (ALMA) dust continuum emission at 344 GHz from the disk in white contours. **f**, Sketch of the d203-506 disk, jet and wind. We note that the low-mass star is not seen in the images because of the disk flaring. All JWST images are from the PDRs4All programme, and the Hubble image is constructed using data from ref. 9.

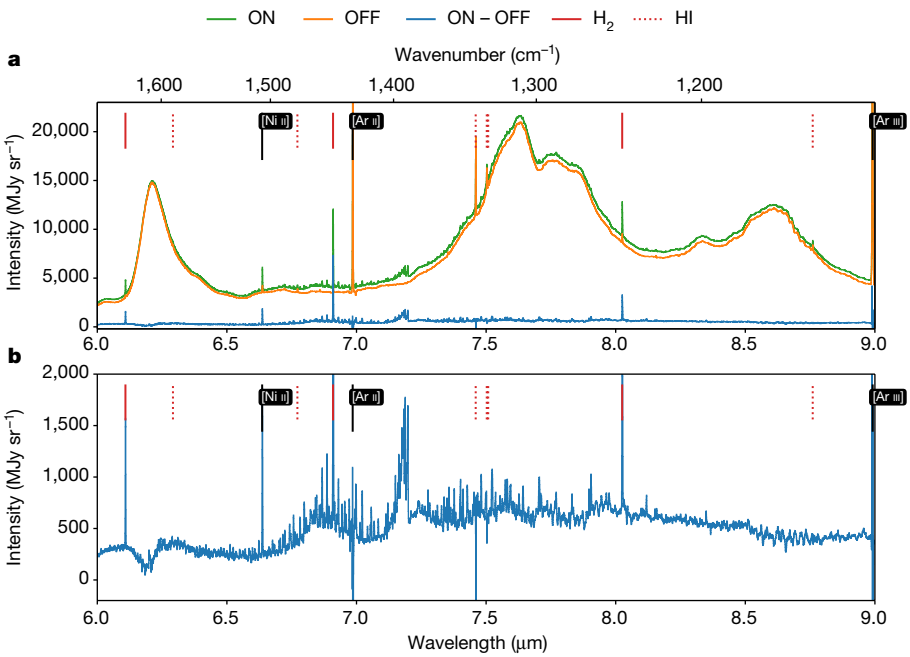

Fig. 2 | JWST-MIRI spectra of d203-506. **a**, Spectrum on the position of d203-506 (ON, green) and close to d203-506 (OFF, orange) over the 6–9 μm MIRI-MRS spectral range. The OFF spectrum is dominated by emission of the Orion Nebula: the broad features at 6.2, 7.7 and 8.6 μm are due to the emission of UV excited PAHs (R. Chown et al., manuscript in preparation). **b**, Spectrum of d203-506 after subtraction of the nebular emission (ON − OFF).

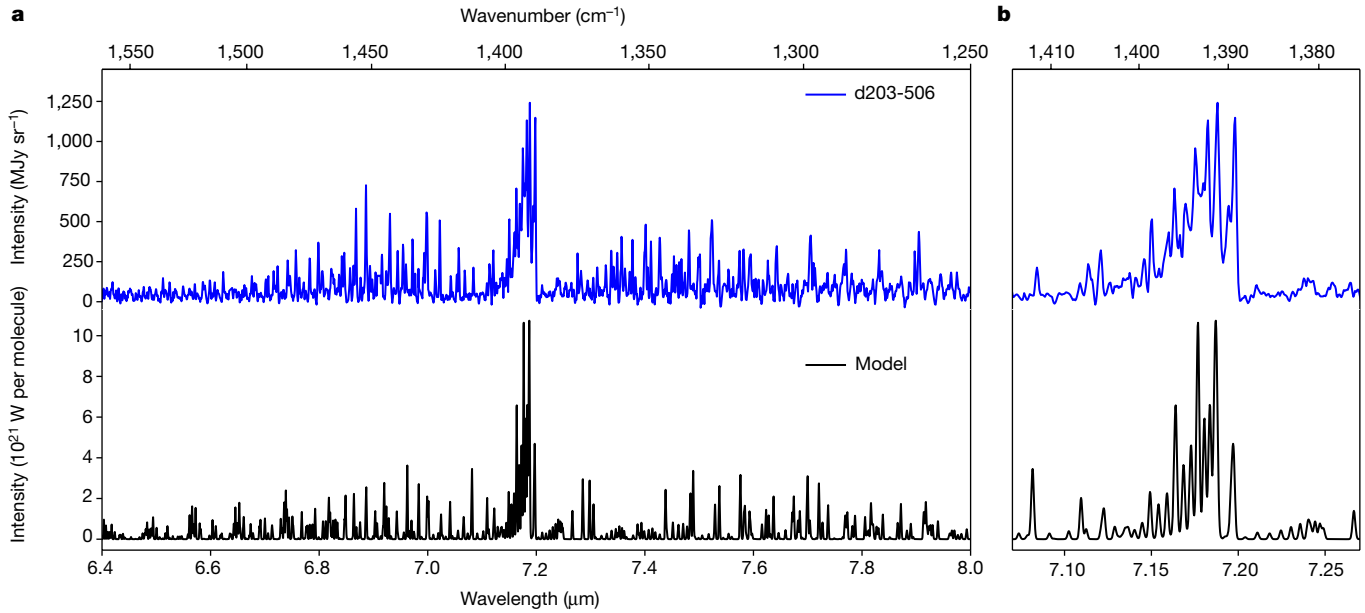

Fig. 3 | Comparison between the observed JWST spectrum of d203-506 and modelled CH_3^+ spectrum. a, Full spectra. **b**, Enlargement of the strongest lines. The model (black curve) for the ν_2 and ν_4 vibrations of CH_3^+ was obtained using the constants in Table 1 (see Methods for a more detailed description of the simulation). A Gaussian linewidth of 0.35 cm^{-1}, corresponding to the MIRI-MRS resolution in this range ($\frac{\lambda}{\Delta\lambda} \approx 3{,}800$, where λ is the wavelength), has been used in the simulation performed using PGOPHER[30]. For clarity, the observational spectrum has been baseline corrected using a spline function and strong individual lines have been removed from the plot: [Ni II] at 6.63 μm, H_2 at 6.92 μm, [Ar II] at 6.99 μm, He I at 7.47 μm and H_2 at 8.02 μm. The standard deviation (1σ) of the noise level is roughly 10 MJy sr^{-1} in this range. The observed lines are 10 to 100 times this noise level.

limit to resolve the structures in d203-506, we cannot fully exclude an emission contribution from the jet.

The 7 μm band visible in Fig. 2 is composed of a succession of narrow features corresponding to ro-vibrational transitions of a molecular carrier. Such insight into the detailed structure of the band is enabled by the unprecedented high spectral resolution and high sensitivity provided by JWST in that spectral region. The presence of these resolved structures, and their spectral span, is compatible with a light molecular carrier. The wavelength coincidence between the observed emission features around 7 μm (Fig. 2) and the ν_2 (out-of-plane bending, 'umbrella' motion) and ν_4 (in-plane bending) bands of CH_3^+ (ref. 12) is striking. Besides CH_3^+, not a single match has been found for a molecule that would possess its shortest wavelength emission signature at 7 μm (details in Methods). Recent laboratory work on the low temperature vibrational spectroscopy of CH_3^+ (ref. 13) finds the vibrational bands match the observed wavelengths. Two more spectroscopic analyses further strengthen the CH_3^+ assignment. First, the intensity pattern of successive emission lines (Fig. 3) is characteristic of the spin statistics of a molecular carrier suggesting three equivalent non-zero-spin atoms (for example, hydrogen atoms), as expected for CH_3^+. Second, the observed emission spectrum can be satisfactorily simulated (Fig. 3) using sets of spectroscopic constants taking values within the range of what is expected from available calculations (refs. 14,15 and this work, Table 1) and laboratory measurements[13]. A detailed description of the spectroscopic analysis procedure is given in the Methods. Quantum number assignments to the ro-vibrational transitions in this spectral range will require both extra theoretical input (notably investigating the Coriolis interaction between the two bands[14]) and laboratory measurements, in particular at even higher resolution and ideally at cold temperature to reduce the spectral density. The higher energy ν_3 band of CH_3^+, situated near 3 μm, has been measured at high resolution in the laboratory[16]. Some of the expected lines from the ν_3 band in this spectral range are tentatively detected with the Near Infrared Spectrograph (NIRSpec) in d203-506 (Supplementary Information and Extended Data Fig. 6). In summary, by spectroscopic standards, CH_3^+ is the best candidate to explain the 7 μm spectral band observed towards the d203-506 protoplanetary disk.

The presence of CH_3^+ in d203-506 raises the question of its origin. Carbon chemistry in these environments typically starts by the radiative association $C^+ + H_2 \rightarrow CH_2^+ + h\nu$, where $h\nu$ is the photon energy. This is a very slow process. The alternative bimolecular reaction $C^+ + H_2(\upsilon = 0) \rightarrow CH^+ + H$, is endothermic by $\Delta E/k_B = 4{,}300$ K, where k_B is the Boltzmann constant[17,18], and thus very slow in cold ($T \cong 100$ K) interstellar gas where $T \ll \Delta E/k_B$. However, strong external FUV radiation fields combined with high gas densities as found in protoplanetary disks open new routes for chemistry. The irradiated gas reaches high temperatures (near 1,000 K, ref. 19) and a substantial fraction of the H_2 molecules are radiatively pumped through fluorescence to vibrationally excited states[20], H_2^* ($\upsilon > 0$). This suprathermal excitation overcomes the endothermicity of reaction in equation (1), allowing H_2^* to

Table 1 | Spectroscopic parameters of CH_3^+ in the two excited states ν_2 and ν_4 from experiment and theory, and comparison with constants from our best model of the observed signatures

Parameter	Unit	ν_2=1		ν_4=1	
		Prediction	Model	Prediction	Model
ν	cm^{-1}	1,372–1,412[a]	1,391	1,373–1,393[b]	1,375
λ	μm	7.289–7.082	7.133	7.283–7.179	7.273
B	cm^{-1}	9.06–9.49[c]	9.37	9.48–9.52[c]	9.50
C	cm^{-1}	4.61–4.66[c]	4.66	4.55–4.65[c]	4.57

The ground-state values (v=0) are kept fixed to the experimental values determined in ref. 16. See Extended Data Table 3 for a more complete set of parameters.

[a]1σ confidence interval from the experimental values of ref. 13 (1,402±10 cm^{-1}) and ref. 12 (1,387±15 cm^{-1}).

[b]1σ confidence interval from the experimental value of ref. 13 (1,383±10 cm^{-1}).

[c]From refs. 14,15 and this work, and scaled to the ground-state parameters of ref. 16 (Extended Data Table 3).

react with C^+, leading to the formation of abundant CH^+ (refs. 21–23). Subsequent fast and exothermic hydrogen abstraction reactions $CH^+ \xrightarrow{H_2} CH_2^+ \xrightarrow{H_2} CH_3^+$ then efficiently lead to CH_3^+. In the Methods section, we quantitatively assess these processes using models, and show that for a wide range of acceptable parameters, CH_3^+ is formed efficiently in FUV-irradiated environments. The formed CH_3^+ reacts very slowly with H_2 (through radiative association) and is mainly destroyed by dissociative recombination with electrons, leading to CH_2, CH and C in comparable amounts[24]. CH_3^+ can also be destroyed by reactions with neutral oxygen producing HCO^+ and with neutral molecules producing molecular ions. These undergo dissociative recombination with electrons yielding complex organic molecules. Therefore, in the presence of UV radiation, gas-phase organic chemistry is initiated through CH_3^+ (refs. 2,3).

The ongoing chemistry in d203-506 described above differs greatly from what has been observed in disks that are not exposed to external UV irradiation where the freeze out of H_2O and CO_2 control the gas composition. In such disks, high abundances of water, HCN, CH_4, C_2H_2 and so on are observed[25,26], species that are not detected in d203-506. In the last decades, the formation of organic molecules in space has been considered to happen mostly at the surface of grains[6,7]. The detection of CH_3^+ indicates that alternative gas-phase routes are available to activate the organic chemistry, when UV radiation is present. Far from being anecdotal, external UV irradiation is expected to occur during the early life of most protoplanetary disks[27], making UV-driven organic chemistry common for the chemical evolution of most protoplanetary disks and of the early Solar System[28,29]. More generally, this chemistry can be active in any environment providing sufficiently high gas density and FUV irradiation ($n_H \gtrsim 10^5$ cm^{-3}, and intensity of the UV radiation field $G_0 \gtrsim 10^4$). This can include, for instance, star-forming regions, the envelopes of planetary nebulae, the inner regions of disks around T-Tauri stars and the interstellar medium of star-forming galaxies near and far. Whereas the CH_3^+ detection presented here is a promising achievement, there are still numerous unanswered questions surrounding the excitation, chemistry and spectroscopic properties of this species (Methods and Supplementary Information). These topics shall be addressed thanks to interdisciplinary scientific efforts that incorporate the expertise of astronomers, physicists and spectroscopists (both laboratory and theory) to fully understand the role of CH_3^+ in organic chemistry in space.

Online content

Any methods, additional references, Nature Portfolio reporting summaries, source data, extended data, supplementary information, acknowledgements, peer review information; details of author contributions and competing interests; and statements of data and code availability are available at https://doi.org/10.1038/s41586-023-06307-x.

1. Black, J. & Dalgarno, A. Models of interstellar clouds. I-the Zeta Ophiuchi cloud. *Astrophys. J. Suppl. Series* **34**, 405–423 (1977).
2. Smith, D. The ion chemistry of interstellar clouds. *Chem. Rev.* **92**, 1473–1485 (1992).
3. Herbst, E. Unusual chemical processes in interstellar chemistry: past and present. *Front. Astronom. Space Sci.* **8**, 776942 (2021).
4. Roueff, E. et al. CH_2D^+, the search for the holy grail. *J. Phys. Chem. A* **117**, 9959–9967 (2013).
5. Indriolo, N., Oka, T., Geballe, T. & McCall, B. J. Constraining the environment of CH^+ formation with CH_3^+ observations. *Astrophys. J.* **711**, 1338 (2010).
6. Cuppen, H. et al. Grain surface models and data for astrochemistry. *Space Sci. Rev.* **212**, 1–58 (2017).
7. Semenov, D. et al. Chemistry in disks-IV. Benchmarking gas-grain chemical models with surface reactions. *Astron. Astrophys.* **522**, A42 (2010).
8. Berné, O. et al. PDRs4All: a JWST early release science program on radiative feedback from massive stars. *Publ. Astron. Soc. Pac.* **134**, 054301 (2022).
9. Bally, J., O'Dell, C. & McCaughrean, M. J. Disks, microjets, windblown bubbles, and outflows in the Orion Nebula. *Astron. J.* **119**, 2919 (2000).
10. Menten, K. M., Reid, M. J., Forbrich, J. & Brunthaler, A. The distance to the Orion Nebula. *Astron. Astrophys.* **474**, 515–520 (2007).
11. Hillenbrand, L. A. & Carpenter, J. M. Constraints on the stellar/substellar mass function in the inner Orion Nebula cluster. *Astrophys. J.* **540**, 236 (2000).
12. Cunha de Miranda, B. K. et al. Threshold photoelectron spectroscopy of the methyl radical isotopomers, CH_3, CH_2D, CHD_2 and CD_3: synergy between VUV synchrotron radiation experiments and explicitly correlated coupled cluster calculations. *J. Phys. Chem. A* **114**, 4818–4830 (2010).
13. Asvany, O., Thorwirth, S., Redlich, B. & Schlemmer, S. Spectroscopy of the low-frequency vibrational modes of CH_3^+ isotopologues. *J. Mol. Spectrosc.* **347**, 1–6 (2018).
14. Kraemer, W. & Špirko, V. Potential energy function and rotation-vibration energy levels of CH_3^+. *J. Mol. Spectrosc.* **149**, 235–241 (1991).
15. Keçeli, M., Shiozaki, T., Yagi, K. & Hirata, S. Anharmonic vibrational frequencies and vibrationally-averaged structures of key species in hydrocarbon combustion: HCO^+, HCO, HNO, HOO, HOO^-, CH_3^+, and CH_3. *Mol. Phys.* **107**, 1283–1301 (2009).
16. Crofton, M. W., Jagod, M., Rehfuss, B. D., Kreiner, W. A. & Oka, T. Infrared spectroscopy of carboions. III. ν_3 band of methyl cation CH_3^+. *J. Chem. Phys.* **88**, 666–678 (1988).
17. Hierl, P. M., Morris, R. A. & Viggiano, A. A. Rate coefficients for the endothermic reactions $C^+ + H_2 \rightarrow CH^+ + H$ as functions of temperature from 400–1300 K. *J. Chem. Phys.* **106**, 10145–10152 (1997).
18. Zanchet, A. et al. $H_2(v=0,1) + C^+(^2P) \rightarrow H + CH^+$ state-to-state rate constants for chemical pumping models in astrophysical media. *Astrophys. J.* **766**, 80 (2013).
19. Champion, J. et al. Herschel survey and modelling of externally-illuminated photoevaporating protoplanetary disks. *Astron. Astrophys.* **604**, A69 (2017).
20. Black, J. H. & van Dishoeck, E. F. Fluorescent excitation of interstellar H_2. *Astrophys. J.* **322**, 412 (1987).
21. Sternberg, A. & Dalgarno, A. Chemistry in dense photon-dominated regions. *Astrophys. J.* **99**, 565 (1995).
22. Agúndez, M., Goicoechea, J. R., Cernicharo, J., Faure, A. & Roueff, E. The chemistry of vibrationally excited H_2 in the interstellar medium. *Astrophys. J.* **713**, 662–670 (2010).
23. Thi, W.-F. et al. Detection of CH^+ emission from the disc around HD 100546. *Astron. Astrophys.* **530**, L2 (2011).
24. Thomas, R. D. et al. Dissociative recombination of vibrationally cold CH_3^+ and interstellar implications. *Astrophys. J.* **758**, 55 (2012).
25. Pontoppidan, K. M. et al. A Spitzer survey of mid-infrared molecular emission from protoplanetary disks. I. Detection rates. *Astrophys. J.* **720**, 887 (2010).
26. Grant, S. L. et al. Minds. the detection of $^{13}CO_2$ with JWST-MIRI indicates abundant CO_2 in a protoplanetary disk. *Astrophys. J. Lett.* **947**, L6 (2022).
27. Winter, A. J. & Haworth, T. J. The external photoevaporation of planet-forming discs. *Euro. Phys. J. Plus* **137**, 1132 (2022).
28. Bergin, E. A., Alexander, C., Drozdovskaya, M., Gounelle, M. & Pfalzner, S. Interstellar heritage and the birth environment of the solar system. Preprint at https://arXiv.org/abs/2301.05212 (2023).
29. Naraoka, H. et al. Soluble organic molecules in samples of the carbonaceous asteroid (162173) Ryugu. *Science* **379**, eabn9033 (2023).
30. Western, C. M. PGOPHER: a program for simulating rotational, vibrational and electronic spectra. *J. Quant. Spectrosc. Radiat. Transf.* **186**, 221–242 (2017).

Methods

Observations and data reduction

The JWST-MIRI-MRS Integral Field Unit data were obtained on 31 January 2023 as part of the JWST Early Release Science 1288 programme (principal investigators: O. Berné, E. Habart, E. Peeters[8]) referred to as PDRs4All. All four channels and the three subchannels were used, covering a wavelength range of 4.9–28 μm at a spectral resolution of 4,000–1,500 (ref. 31). The observations are centred on right ascension (RA) = 05 h 35 min 20.4749 s at a declination of −5° 25′, 10.45″ and span a mosaic of nine pointings. The overall science exposure time is 14,086.11 s for the whole mosaic. We used the FASTR1 readout mode with four-point dithering. We reduced the data using the JWST Data Reduction pipeline v.1.9.5. The stage 2 residual fringe correction was applied in addition to the standard fringe correction step. A master background subtraction was applied in stage 3 of the reduction. At the end of the data reduction, we obtained four MIRI datacubes, one for each channel, each channel containing its three corresponding subchannels (short, medium and long). The details of the data reduction for MIRI-Integral Field Unit is part of a dedicated paper by the PDRs4All team (R. Chown et al., manuscript in preparation).

In this paper, we also use one narrow band image of the NIRSpec observations of the same object as well as a NIRCam filter. Specifically, we use the NIRCam F212N filter image and the NIRSpec spectral cube corresponding to the F290LP filter that spans from roughly 2.9 to 5 μm. Observations were obtained with JWST-NIRSpec (JWST-NIRCam) on 10 September 2022 and reduced using the JWST pipeline v.1.9.4 (1.7.1) with Calibration Reference Data System context file jwst_1014.pmap (jwst_0969.pmap). For the NIRCam observations, no OFF emission was subtracted. For the NIRSpec observations, a dedicated OFF observation was subtracted. The details of the data reduction for these two instruments is discussed in a dedicated paper by the PDRs4All team on NIRCam (E. Habart et al., manuscript in preparation) and NIRSpec (E. Peeters et al., manuscript in preparation). The details on the observing strategy can be found in ref. 8.

Data analysis

To work with complete spectra spanning all the MIRI-MRS wavelength range of 4.9–28 μm, we first stitch the spectra of the four channels to remove jumps between spectral orders. For each spectrum, we arbitrarily choose the one from channel 2 long as a reference. Shorter and longer wavelengths (channels 1, 3 and 4) are thus scaled accordingly. We create (with numpy) an array of wavelengths spanning the full wavelength range, that is, between 4.900 and 27.901 μm, with 50,000 points and a constant step. Each channel spectrum is then interpolated onto this grid and jumps are removed by scaling each spectral order based on the average flux in the overlap region. The integrated intensity is conserved in this procedure, and uncertainties propagated.

The two extracted spectra shown in blue and orange in Fig. 2 are from the 'ON' and 'OFF' positions, respectively. The ON (OFF) spectrum were extracted from an ellipse (circular aperture) centred on the position α = 05 h 35 min 20.357 s, δ = −5° 25′ 5.81″ (α = 05 h 35 min 20.370 s, δ = −5° 25′ 4.97″), with dimensions of l = 0.52″, h = 0.38″ (of radius r = 0.365″) and a position angle of +33° (trigonometric) with respect to north. To have the emission of d203-506 we choose to subtract the nebula emission by evaluating ON − OFF. The ON and OFF spectra over the full MIRI-MRS range are shown in Extended Data Fig. 1, and the full subtracted spectrum is shown in Extended Data Fig. 2. In Extended Data Fig. 2, some lines are negative because of the over-subtraction of ionized emission lines that dominate in the nebula but are absent in d203-506. Some polycyclic aromatic hydrocarbon (PAH) bands are seen in negative in the ON–OFF spectrum; this is because of intrinsic variation of the PAH bands due to, for example, size or ionization, and this cannot be interpreted as PAH absorption.

Line identification

Using the ON–OFF spectrum described previously and the line list provided by the PDRs4All Early Release Science team[8], we identified the strong emission lines present in the data. The main emission lines are from H I and H_2 and are listed in Extended Data Tables 1 and 2, respectively. The H_2 lines intensities presented in the latter table are measured using a Gaussian fitting to the observed lines, and the wavelength of the H_2 transition from ref. 32. The approach to fit the observed lines is presented in ref. 33. Nebular emission lines from atomic ions are also identified and are shown in Fig. 2 and Extended Data Fig. 2 with black vertical lines with their names in the attached box. In addition, several OH lines are also identified between 9 and 11 μm and are shown as green vertical lines on the same figures. For this wavelength range, we used OH wavelengths from refs. 34 and 35. The study of OH emission in d203-506 will be the subject of a forthcoming paper (M. Zannese et al., manuscript in preparation).

From the H_2 lines listed in Extended Data Table 2 we derive an excitation diagram, using the H_2 Toolbox[36] developed as part of the PDRs4All project science enabling products (https://pdrs4all.org/seps/). This is a tool for fitting temperature, column density and *ortho*-to-*para* ratio in H_2 excitation diagrams. A one or two temperature model is assumed, and the fit finds the excitation temperatures and column densities, and optionally *ortho*-to-*para* ratio. The source code is available at https://dustem.astro.umd.edu/tools.html. The result of this analysis is shown in Extended Data Fig. 3. The derived excitation temperature is T_{ex} = 923 ± 48.2 K.

Other candidate molecules

There are no unassigned series of lines observed in the 5.2–6.2 μm range, corresponding to C=O or C≡N vibrations (Fig. 2) thus excluding most small species containing these chemical functions as carrier of the observed 7 μm features. At longer wavelengths (8–17 μm, Extended Data Fig. 2), the spectrum is devoid of strong unassigned emission lines. Many hydrocarbon molecules, radicals and ions (for example, CH_2, CH_2^+, and so on) possess low frequency modes and would thus emit in that range. Instead, the lowest vibrational modes of CH_3^+ lie at 7 μm. We thoroughly inspected the literature data on other hydrocarbons and known interstellar species (both neutral and charged) for possible matches and used local thermodynamic equilibrium models to predict the emission from molecules in this spectral range. The tested molecules include—not exhaustively—H_2O (and isotopologues), H_2O^+, NH_4^+, C_2H_2, CH_3, HCN, SO_2, all hydrocarbons present in the HITRAN database[37], NH_3, CH_3OH and CH_3CN.

Spectroscopy of the methyl cation

CH_3^+ is a planar molecule belonging to the D_{3h} group of symmetry. It possesses four fundamental modes of vibration following an irreducible representation $\Gamma = 1\,A_1' + 1\,A_2'' + 2E'$ (the two E′ modes are doubly degenerate). It is an oblate symmetric-top molecule for which rotational energy levels of non-degenerate vibrational states are described with two quantum numbers, J, the total angular-momentum quantum number excluding nuclear spin and K, the projection of **N** (the total angular momentum excluding nuclear and electron spins) along the principal axis of symmetry; an extra l quantum number accounts for Coriolis coupling in degenerate vibrational states (l = ±1 in υ_4 = 1). The energy levels in a given vibronic state can be calculated using the energy of the vibronic state, two rotational constants ($A = B$ and C), centrifugal distortion parameters (D_J, D_{JK}, D_K, and so on) and, for states of E′ symmetry, further Coriolis coupling and l-doubling parameters (ζ, η_J, q). The molecule possesses three equivalent hydrogen atoms (fermions, I_H = 1/2) resulting in spin-statistical weights of (0, 0, 4, 4, 2, 2) for the levels of the states of symmetries (A_1', A_1'', A_2', A_2'', E′, E″)[38]. In the following, we used the PGOPHER software[30] to simulate the ro-vibrational spectrum of CH_3^+.

As no experimental information is available on the $\upsilon_2 = 1$ (A_2'' symmetry) and $\upsilon_4 = 1$ (E′ symmetry) states of CH_3^+, except the band positions[12,13], we rely on quantum chemical calculations to estimate the rotational constants in these excited states. We carried out geometry optimization and anharmonic frequency analysis at the ωB97X-D/cc-pVQZ level of theory[39–41] using the Gaussian 16 suite of electronic structure programs[42]. The main results from these calculations are reported in Extended Data Table 3. The table also contains the calculated constants reported in the literature[14,15]. As well as the rotational constants, the quantum chemical calculations also give us insights about the transition moments of the ν_2 (out-of-plane bending, 'umbrella' motion) and ν_4 (in-plane bending) bands. Our calculations predict transition moments of 0.084 and 0.064 D for ν_2 and ν_4, respectively. Such low values have to be taken with caution as experimental values can differ significantly, by 0.1 D or more. Nevertheless, these values are consistent with the small values obtained by CCSD(T)/cc-pwCVTZ calculations performed in course of the work presented in ref. 13 (0.06 and 0.07 D, respectively), as well as those reported in ref. 43 (0.049 and 0.111 D) and ref. 44 (0.10 and 0.16 D).

To assess the reliability of the spectroscopic constants derived from the different quantum chemical calculations (both from this work and the literature), the calculated values in $\upsilon = 0$ and $\upsilon_3 = 1$ were compared to the experimental values of the ν_3 band. Transitions within the ν_3 band (asymmetric stretching) observed by Crofton et al.[16] were fitted in the present work using PGOPHER (so as to use the same model for ν_3 and ν_2/ν_4) leading to the spectroscopic parameters reported in Extended Data Table 3. These derived parameters are in excellent agreement with those reported in ref. 16. They also are in very good agreement with the parameters obtained by the anharmonic calculations from this study. These results were used to scale the calculated constants in $\upsilon_2 = 1$ and $\upsilon_4 = 1$ according to the formula $B_{\text{scaled }\upsilon_i} = B_{\text{calc }\upsilon_i} \times B_{\exp \upsilon_3=1}/B_{\text{calc }\upsilon_3=1}$, where $B_{\text{calc }\upsilon_i}$ is the calculated value of B at a frequency ν_i, $B_{\exp \upsilon_3=1}$ is the experimental value of B, and $B_{\text{calc }\upsilon_3=1}$ is the calculated value of B for $\upsilon_3 = 1$ (and similarly for C). For the rotational constants calculated in ref. 14, because no calculated values in $\upsilon_3 = 1$ are reported, the scaling was made using values in $\upsilon = 0$. The scaled values appear in blue in Extended Data Table 3; they serve as a range of confidence for the spectral simulations.

Despite our best efforts, no definite spectroscopic analysis of the bands observed by JWST was achieved, that is, we could not assign with confidence quantum numbers to the observed transitions. Instead, we performed several simulations by varying the rotational constants of $\upsilon_2 = 1$ and $\upsilon_4 = 1$ until qualitative agreement with the observational data was achieved. Such qualitative agreement was assessed using the following criteria (by decreasing order of importance): (1) Q-branch line position and intensity; (2) P- and R-branch spread and spectral line density and (3) line positions and intensities in the P and R branches. In all cases, the Coriolis interaction constants were kept fixed to the calculated values, and so were the transition moments of the ν_2 and ν_4 bands. This leads us to produce four models, I to IV (Extended Data Table 3 and Extended Data Figs. 4 and 5; model III being the model presented in the main article), which reasonably reproduce the astronomical data. It is worth noting, however, that the spectral density is greater on the spectrum of d203-506 than in our simulations, which could either reflect the presence of another species, or some discrepancies in the rotational constants used in models I to IV. Regarding the temperature, for all models, a rotational temperature of 400 K seems to adequately simulate the astronomical features (that is, the spread of the P, Q and R branches). Higher temperatures lead to P and R branches that spread further than what is observed in the astronomical spectrum. Whereas the simulations were performed under the assumption of thermal equilibrium, astronomical excitation conditions may differ significantly (see detailed discussion in the following section). This is particularly relevant to the relative intensities of the ν_2 and ν_4 bands, as the $\upsilon_2 = 1$ and $\upsilon_4 = 1$ vibrational states may be populated differently in d203-506.

We have also investigated the presence of lines emanating from the ν_3 band of CH_3^+ near 3 μm in the NIRSpec data of d203-506 (O. Berné et al., manuscript in preparation). The ν_3 band has been observed at high resolution in the laboratory by refs. 16,45. Using the constants derived from these observations, we computed a synthetic spectrum of the ν_3 band at 400 K and compare it to the NIRSpec background subtracted spectrum (using the same apertures as for MIRI, Methods) in Extended Data Fig. 6. The predicted lines are found to coincide with lines in the observations.

In summary, high-resolution laboratory infrared spectra of CH_3^+ in the 7 μm region are needed to identify individual transitions in the astronomical data. First laboratory measurements at low temperatures will initiate this process, hopefully deciphering the strong Coriolis coupling between the degenerate ν_2 and ν_4 vibrations of CH_3^+. To support a quantitative analysis of the astronomical spectra, laboratory studies also conducted at higher temperatures are required.

Chemistry of the methyl cation

We modelled the photochemistry in the strongly FUV-irradiated photoevaporative wind and upper disk layers of d203-506 using the Meudon Photodissociation Region code[46]. The code solves the FUV radiative transfer in a medium of gas and dust[47], as well as the steady-state heating, cooling, chemistry and H_2 (υ, J) level populations as a function of depth into the neutral disk (in magnitude (mag) of visual extinction A_V). Berné et al. (manuscript in preparation) used this code to reproduce the H_2 line intensities detected by JWST-NIRSpec and obtained a radiation field intensity $G_0 \cong 4 \times 10^4$ and a gas density $n_H = n(H) + 2n(H_2) \cong 10^{5-6}$ cm^{-3}. We first adopt $n_H = 3.5 \times 10^5$ and use an extinction law suited to the Orion molecular cloud[48], and consistent with dust grains ($R_V = 5.62$ and $N_H/E(B-V) = 1.05 \times 10^{22}$ cm^{-2}) bigger than in standard diffuse interstellar clouds ($R_V = 3.1$). This choice leads to a FUV dust extinction cross-section, $\sigma_{1,000A}(\text{FUV}) = 1.1 \times 10^{-21}$ cm^{-2} per H a factor of about two smaller than standard interstellar medium grains. In addition, we run models adopting 'bigger grains' (by a factor of about four), leading to $\sigma_{1,000A}(\text{FUV}) = 7 \times 10^{-22}$ cm^{-2} H^{-1}. This smaller FUV cross-section is compatible with the kind of dust grains expected in the upper layers of protoplanetary disks[49].

Extended Data Fig. 7 shows the predicted density and temperature structure of the wind and upper disk layers (upper panels) as well as the C^+, CH^+, CH_2^+, CH_3^+, CO and HCO^+ abundance profiles (lower panels). Extended Data Fig. 7a refers to models using 'Orion grains' and $n_H = 3.5 \times 10^5$ cm^{-3} . The other plots refer to models adopting bigger grains and densities of 3.5×10^5 cm^{-3} (Extended Data Fig. 7b), 3.5×10^6 cm^{-3} (Extended Data Fig. 7c) and 10^7 cm^{-3} (Extended Data Fig. 7d). The last ones are more representative of the outer layers of a disk[50].

In all these models, reaction $C^+ + H_2(\upsilon, J) \rightarrow CH^+ + H$ (equation (1)) drives the formation of CH^+ as soon as the H_2 abundance rises. In these conditions, high temperatures and presence of FUV-pumped vibrationally excited H_2^*, reaction in equation (1) is much faster than the slow radiative association reactions $C^+ + H_2 \rightarrow CH_2^+ + \text{photon}$ and $C^+ + H \rightarrow CH^+ + \text{photon}$. These radiative associations produce small amounts of CH_2^+ and CH^+ in cold gas ($T < 100$ K). Our models include an $H_2(\upsilon, J)$ state-dependent treatment of equation (1) (ref. 18), appropriate to the non-thermal populations of H_2^* in FUV-irradiated environments. In particular, the CH^+ formation rate is computed by summing over all formation rates for each specific state of H_2. Once CH^+ is formed, fast and exoergic hydrogen abstraction reactions $CH^+ \xrightarrow{H_2} CH_2^+ \xrightarrow{H_2} CH_3^+$ $CH_2^+ \xrightarrow{H_2} CH_3^+$ lead to CH_3^+. The efficiency of this chemical pipe to CH_3^+ depends on the abundance of H atoms in the gas (because they readily react with CH^+, ref. 51) and that of electrons (because they destroy CH_2^+ and CH_3^+). Reactions with atomic hydrogen dominate CH^+ destruction when the molecular gas fraction, defined as $f_{H_2} = 2n(H_2)/n_H$, is less than or equal to 0.5 ($f_{H_2} = 1$ when all hydrogen is in molecular form). All models in Extended Data Fig. 7 predict that the CH_3^+

abundance peaks close to the H/H_2 transition, at $A_V \cong 1$ mag, where $T \cong 1{,}000$–800 K. Extended Data Fig. 8 summarizes the dominant chemical reactions at the CH_3^+ abundance peak. We note that the CH^+ and CH_3^+ abundance profiles roughly follow the density profile of vibrationally excited H_2^* (dotted black curve in the upper panel of Extended Data Fig. 7). Hence, irrespective of the exact gas density value, the infrared H_2 lines detected with JWST in d203-506 probe strongly FUV-irradiated hot gas, where CH^+ and CH_3^+ efficiently form.

Our models predict $N(CH_3^+)/N(CH^+)$ column density ratios of roughly equal to 1–15 (increasing as n_H increases). We note that the bulk column density of these species stem from FUV-illuminated gas at $A_V < 3$ mag. Deeper inside, their abundances drop by orders of magnitude. Hence, both CH^+ and CH_3^+ are chemical tracers of the most irradiated wind and upper disk layers.

The local CH^+/CH_3^+ abundance ratio can be analytically estimated from the following network of gas-phase chemical reactions:

$$C^+ + H_2(v,J) \rightarrow CH^+ + H \quad (1)$$

$$CH^+ + H \rightarrow C^+ + H_2 \quad (2a)$$

$$CH^+ + H_2 \rightarrow CH_2^+ + H \quad (2b)$$

$$CH_2^+ + H_2 \rightarrow CH_3^+ + H \quad (3)$$

$$CH_2^+ + e^- \rightarrow \text{products} \quad (4)$$

$$CH_3^+ + e^- \rightarrow \text{products} \quad (5)$$

We note that adopting the photodissociation rate of ref. 52, CH_3^+ photodissociation is expected to be much slower than dissociative recombination with electrons even in strong UV fields. Therefore, in steady state, one obtains the ratio of abundances x:

$$\frac{x(CH_3^+)}{x(CH^+)} = \frac{k_{2b} f_{H_2}^2}{2k_5\, x_e (f_{H_2} + 2x_e\, k_4/k_3)} \simeq \frac{k_{2b}}{2k_5\, x_e} f_{H_2} \quad (6)$$

where $x_e = n(e^-)/n_H$ is the electron abundance. In the last step we assumed that CH_2^+ destruction by reactions with H_2 are much faster than dissociative recombinations with electrons at the CH_3^+ abundance peak (as confirmed by the model). In our model we used the following reaction rate coefficients: $k_{2b} = 1.2 \times 10^{-9}$ cm^3 s^{-1} (ref. 53), $k_3 = 1.6 \times 10^{-9}$ cm^3 s^{-1} (ref. 54), $k_4 = 6.40 \times 10^{-7}(T/300)^{-0.60}$ cm^3 s^{-1} (ref. 55) and $k_5 = 6.97 \times 10^{-7}(T/300)^{-0.61}$ cm^3 s^{-1} (ref. 24). Using representative values for the wind and upper disk layers of d203-506; $T = 900$ K and $x_e \cong x(C^+) \cong 1.4 \times 10^{-4}$, one obtains $x(CH_3^+)/x(CH^+) \cong 12\, f_{H_2}$ from equation (1). This analytical abundance ratio agrees with the detailed predictions of our photochemical models. That is, the chemical reactions in equations (1)–(6) dominate the formation of CH_3^+ in FUV-irradiated gas. In particular, models predict that the CH_3^+ abundance peaks at gas molecular fractions of $f_{H_2} = 0.3$–0.5 (pink dotted curves in Extended Data Fig. 7).

The reaction in equation (5) produces CH_2, CH and C in similar amounts[24]. These are key reactive intermediate species that trigger the chemistry of carbon species[56]. In addition, reaction $O + CH_3^+ \rightarrow HCO^+ + H_2$ (ref. 57) is a dominant source of HCO^+, and thus of CO, in these irradiated hot gas layers (Extended Data Fig. 7 also shows the predicted HCO^+ abundance profile in the photoevaporative wind and upper disk layers). The morphology of the observed $HCO^+ J = 4$-3 line emission (first detected by ref. 19 and then mapped with ALMA at high angular resolution by Berné et al. (manuscript in preparation)) resembles that of vibrationally excited H_2 and CH_3^+ observed with JWST (O. Berné et al., manuscript in preparation). It will be difficult to explain the presence of extended HCO^+ emission in these strongly irradiated gas layers without the FUV-driven chemistry described here and tested by the presence of CH_3^+. We note that this hot HCO^+ linked to the extended H_2^* emission is different from the HCO^+ present in lower and denser layers of protoplanetary disks and formed by standard ion-molecule chemistry[50].

Specific two-dimensional models, better adapted to the geometry of the upper disk layers and FUV-irradiated wind, will be needed to fully understand the density structure and abundance distribution of the observed molecular emission with JWST.

Data availability

The JWST data presented in this paper are publicly available through the MAST online archive (http://mast.stsci.edu) using the PID 1288. The MIRI spectra presented in Fig. 2 and Extended Data Figs. 1 and 2 are available in ASCII format at https://doi.org/10.5281/zenodo.7989669 (ref. 59). The PGOPHER files to create the model spectra of CH_3^+ are available via https://doi.org/10.5281/zenodo.7993330 (ref. 60). Source data are provided with this paper.

Code availability

The JWST pipeline used to produce the final data products presented in this article is available at https://github.com/spacetelescope/jwst. The MEUDON PDR code is publicly available at https://ism.obspm.fr/pdr_download.html.

31. Labiano, A. et al. Wavelength calibration and resolving power of the JWST MIRI medium resolution spectrometer. *Astron. Astrophys.* **656**, A57 (2021).
32. Roueff, E. et al. The full infrared spectrum of molecular hydrogen. *Astron. Astrophys.* **630**, A58 (2019).
33. Foschino, S., Berné, O. & Joblin, C. Learning mid-IR emission spectra of polycyclic aromatic hydrocarbon populations from observations. *Astron. Astrophys.* **632**, A84 (2019).
34. Tabone, B., van Hemert, M. C., van Dishoeck, E. F. & Black, J. H. OH mid-infrared emission as a diagnostic of H_2O UV photodissociation. I. Model and application to the HH 211 shock. *Astron. Astrophys.* **650**, A192 (2021).
35. Zannese, M. et al. OH mid-infrared emission as a diagnostic of H_2O UV photodissociation. II. Application to interstellar photodissociation regions. *Astron. Astrophys.* **671**, A41 (2023).
36. Pound, M. W. & Wolfire, M. G. The photodissociation region toolbox: software and models for astrophysical analysis. *Astron. J.* **165**, 25 (2022).
37. Gordon, I. et al. The HITRAN2020 molecular spectroscopic database. *J. Quant. Spectrosc. Rad. Trans.* **277**, 107949 (2022).
38. Schulenburg, A. M., Alcaraz, C., Grassi, G. & Merkt, F. Rovibrational photoionization dynamics of methyl and its isotopomers studied by high-resolution photoionization and photoelectron spectroscopy. *J. Chem. Phys.* **125**, 104310 (2006).
39. Chai, J.-D. & Head-Gordon, M. Long-range corrected hybrid density functionals with damped atom–atom dispersion corrections. *Phys. Chem. Chem. Phys.* **10**, 6615 (2008).
40. Dunning, T. H. Gaussian basis sets for use in correlated molecular calculations. I. The atoms boron through neon and hydrogen. *J. Chem. Phys.* **90**, 1007–1023 (1989).
41. Woon, D. E. & Dunning, T. H. Gaussian basis sets for use in correlated molecular calculations. III. The atoms aluminum through argon. *J. Chem. Phys.* **98**, 1358–1371 (1993).
42. Frisch, M. J. et al. Gaussian 16 Revision A.01 (Gaussian, Inc., 2016).
43. Pracna, P., Spirko, V. & Kraemer, W. Ab initio study of linestrengths of vibration-rotation transitions of ammonia and methyl cations. *J. Mole. Spectrosc.* **158**, 433–444 (1993).
44. Nyman, G. & Yu, H.-G. Infrared vibrational spectra of CH_3^+ and its deuterated isotopologues. *AIP Adv.* **9**, 095017 (2019).
45. Jagod, M.-F., Gabrys, C. M., Rösslein, M., Uy, D. & Oka, T. Infrared spectrum of CH_3^+ involving high rovibrational levels. *Can. J. Phys.* **72**, 1192–1199 (1994).
46. Le Petit, F., Nehmé, C., Le Bourlot, J. & Roueff, E. A model for atomic and molecular interstellar gas: the Meudon PDR code. *Astrophys. J. S.* **164**, 506–529 (2006).
47. Goicoechea, J. R. & Le Bourlot, J. The penetration of far-UV radiation into molecular clouds. *Astron. Astrophys.* **467**, 1–14 (2007).
48. Cardelli, J. A., Clayton, G. C. & Mathis, J. S. The relationship between infrared, optical, and ultraviolet extinction. *Astrophys. J.* **345**, 245 (1989).
49. Birnstiel, T. et al. The Disk Substructures at High Angular Resolution Project (DSHARP). V. Interpreting ALMA maps of protoplanetary disks in terms of a dust model. *Astrophys. J. Lett.* **869**, L45 (2018).
50. Walsh, C., Millar, T. J. & Nomura, H. Molecular line emission from a protoplanetary disk irradiated externally by a nearby massive star. *Astrophys. J. Lett.* **766**, L23 (2013).
51. Plasil, R. et al. Reactions of cold trapped CH^+ ions with slow H atoms. *Astrophys. J.* **737**, 60 (2011).
52. Blint, R. J., Marshall, R. F. & Watson, W. D. Calculations of the lower electronic states of CH_3^+: a postulated intermediate in interstellar reactions. *Astrophys. J.* **206**, 627–631 (1976).
53. McEwan, M. J. et al. New H and H_2 reactions with small hydrocarbon ions and their roles in benzene synthesis in dense interstellar clouds. *Astrophys. J.* **513**, 287–293 (1999).

54. Adams, N. & Smith, D. Reactions of hydrocarbon ions with hydrogen and methane at 300 K. *Chem. Phys. Lett.* **47**, 383–387 (1977).
55. Larson, A. et al. Branching fractions in dissociative recombination of CH_2^+. *Astrophys. J.* **505**, 459–465 (1998).
56. Cuadrado, S. et al. The chemistry and spatial distribution of small hydrocarbons in UV-irradiated molecular clouds: the Orion Bar PDR. *Astron. Astrophys.* **575**, A82 (2015).
57. Scott, G. B. I., Milligan, D. B., Fairley, D. A., Freeman, C. G. & McEwan, M. J. A selected ion flow tube study of the reactions of small $C_mH_n^+$ ions with O atoms. *J. Chem. Phys.* **112**, 4959–4965 (2000).
58. Argyriou, I. et al. JWST MIRI flight performance: the medium-resolution spectrometer. *Astron. Astrophys.* **675**, A111 (2023).
59. Schroetter, I. & The PDRs4All team. JWST MIRI channel1 spectrum of d203-506. *Zenodo* https://doi.org/10.5281/zenodo.7989669 (2023).
60. Martin, M. A., Jacovella, U. & Gans. B. p-Gopher files for the CH_3^+ v_4/v_2 and v_3 bands. *Zenodo* https://doi.org/10.5281/zenodo.7993330 (2023).

Acknowledgements O.B. is funded by a CNES APR programme. MIRI data reduction is performed at the French MIRI centre of expertise with the support of CNES and the ANR-labcom INCLASS between IAS and the company ACRI-ST. Part of this work was supported by the Programme National Physique et Chimie du Milieu Interstellaire (PCMI) of CNRS/INSU with INC/INP cofunded by CEA and CNES. Quantum chemical calculations were performed using HPC resources from the 'Mésocentre' computing centre of CentraleSupélec and École Normale Supérieure Paris-Saclay supported by CNRS and Région Ile-de-France (http://mesocentre.centralesupelec.fr/). J.R.G. and S.C. thank the Spanish MCINN for funding support under grant no. PID2019-106110GB-I00. J.C and E.P. acknowledge support from the University of Western Ontario, the Institute for Earth and Space Exploration, the Canadian Space Agency and the Natural Sciences and Engineering Research Council of Canada. The Cologne spectroscopy group acknowledges funding by the Deutsche Forschungsgemeinschaft DFG (CRC956, subproject B2, ID no. 184018867) and the ERC AdG Missions (ID no. 101020583). Work by Y.O. and M. Röllig is carried out within the Collaborative Research Centre 956, subproject C1, funded by the DFG - project ID no. 184018867. C.B. is grateful for an appointment at NASA Ames Research Center through the San José State University Research Foundation (grant no. 80NSSC22M0107). T.O. acknowledges support from JSPS Bilateral Programme, grant no. 120219939. A.F. thanks Spanish MICIN for funding support from PID2019-106235GB-I00.

Author contributions O.B. found the signal in the data and led the analysis of the data and write-up of the article. M.-A.M.-D., I.S., U.J., B.G., E.D., L.H.C., E.B., F.A., J.C., E.R., J.H.B., O.A., C.J., S.S., S.T., J.C., M.G., A.T., T.O. and M.Z. conducted the spectroscopic analysis and participated in the write-up. M.-A.M.-D. created Fig. 3, and Extended Data Figs. 4 and 5. I.S. created Figs. 1 and 2 and Extended Data Figs. 1–3. I.S. and O.B. created Extended Data Fig. 6. J.R.G. performed the chemical models, created Extended Data Figs. 7 and 8, and participated in the write-up. O.B., E.H. and E.P. led the JWST observing programme. I.S., J.R.G., E.D., E. Bergin, F.A., J.C., A.C., B.T., C.J., A.T., M.Z., A.A., J.B.-S., C.B., E. Bron, R.C., S.C., D.D., M.E., A.F., K.D.G., L.I., O.K., B.K., O.L., D.L., R.L.G., A.M., R.M., Y.O., T.O., S.P., M.W.P., M. Robberto, M. Röllig, B.S., T.S., A.S., B.T., D.V.D.P., S.V. and M.G.W. contributed to the observing programme with JWST. I.S., A.C., R.C., A.S., B.T., F.A., D.V.P. reduced the data. E.D., M.-A.M.-D., L.H.C., J.R.G. and O.B. conducted the column density analysis. J.H.B. wrote the section on the excitation of CH_3^+. M.G.W. and J.H.B. corrected the English throughout the manuscript. All authors contributed to the discussions and provided feedback on the manuscript.

Competing interests The authors declare no competing interests.

Additional information
Supplementary information The online version contains supplementary material available at https://doi.org/10.1038/s41586-023-06307-x.
Correspondence and requests for materials should be addressed to Olivier Berné.
Peer review information *Nature* thanks Daniel Harsono, Stephen Lepp and the other, anonymous, reviewer(s) for their contribution to the peer review of this work.

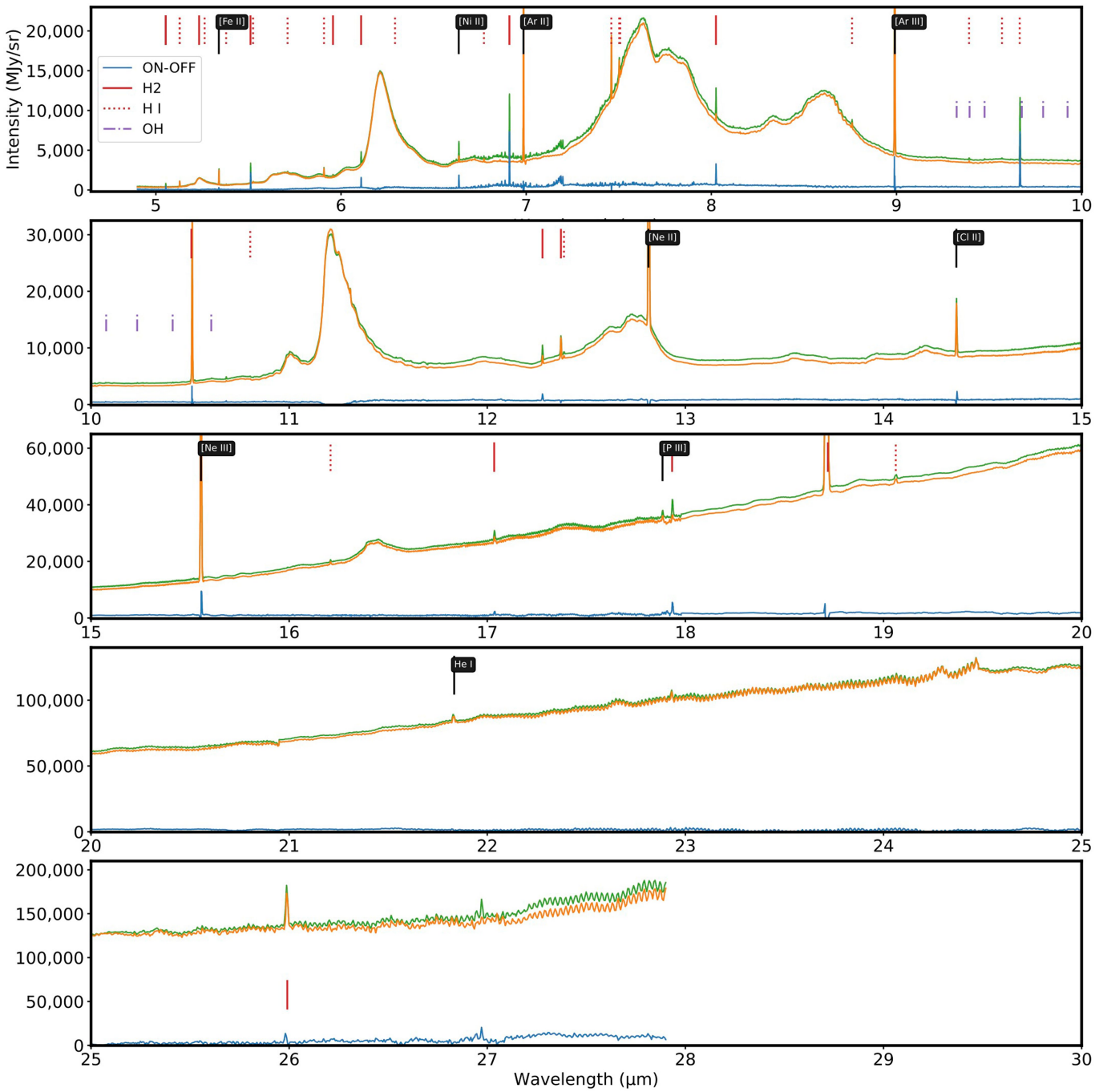

Extended Data Fig. 1 | ON and OFF spectra of d203-506 over the full MIRI-MRS spectral range. The ON-OFF spectrum is also shown. Main atomic and H_2 lines are indicated.

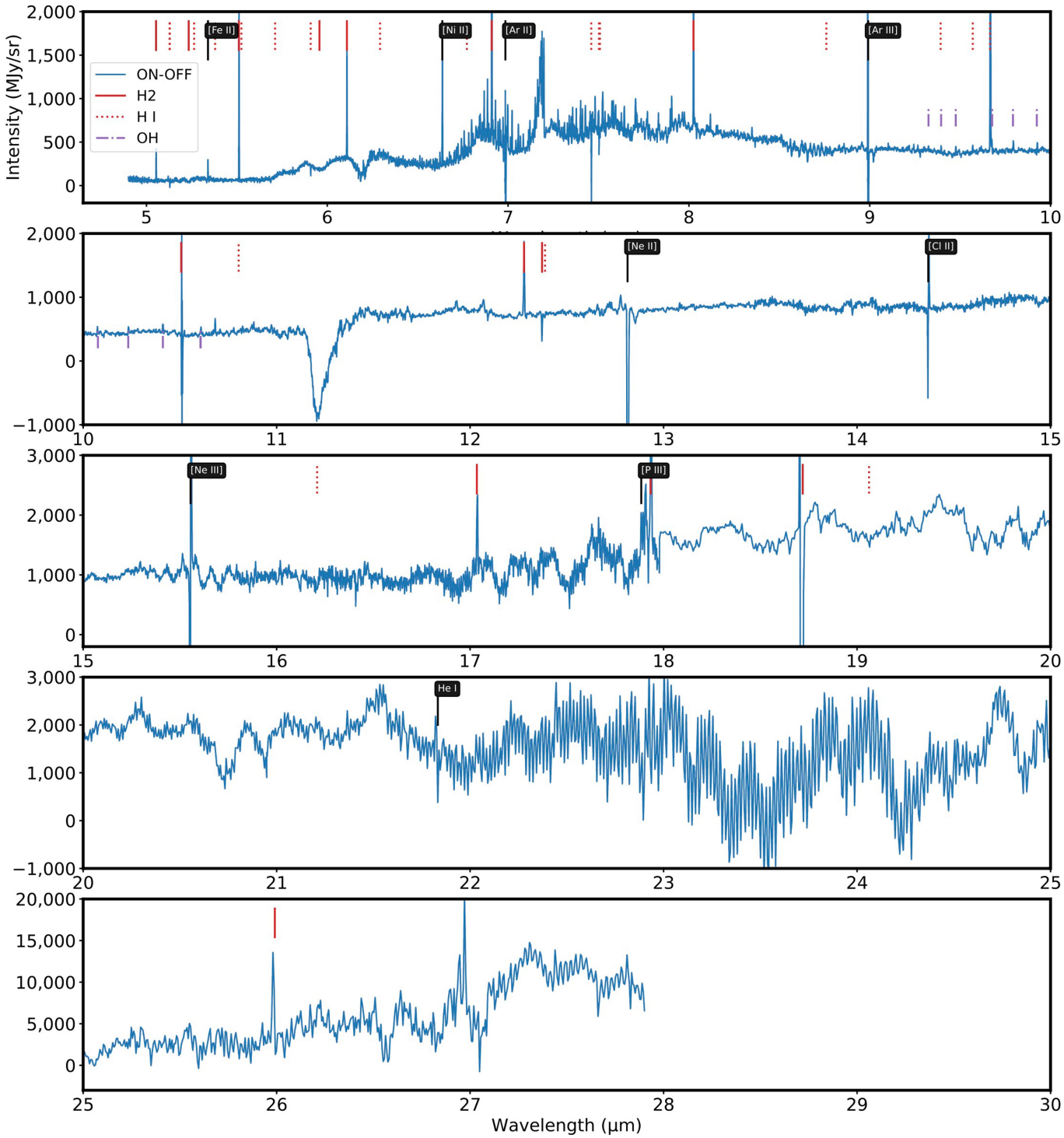

Extended Data Fig. 2 | ON-OFF spectrum of d203-506 over the full MIRI-MRS spectral range. Main atomic and H_2 lines are indicated.

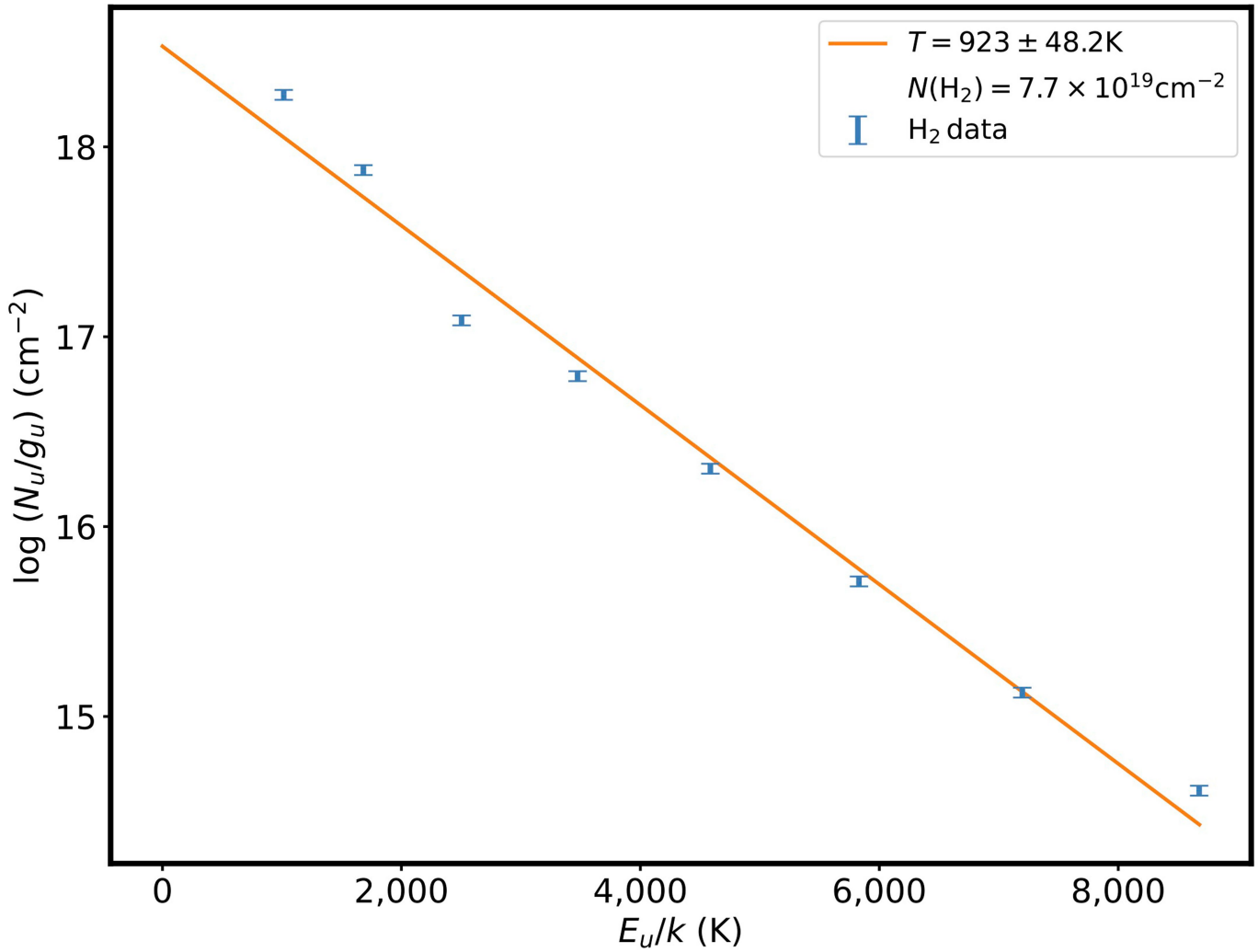

Extended Data Fig. 3 | H_2 excitation diagram derived from the line intensities in Extended Data Table 2 using the H_2 toolbox (see Methods for details). Error bars result from the propagation of the absolute calibration error of MIRI, which we take from ref. 58.

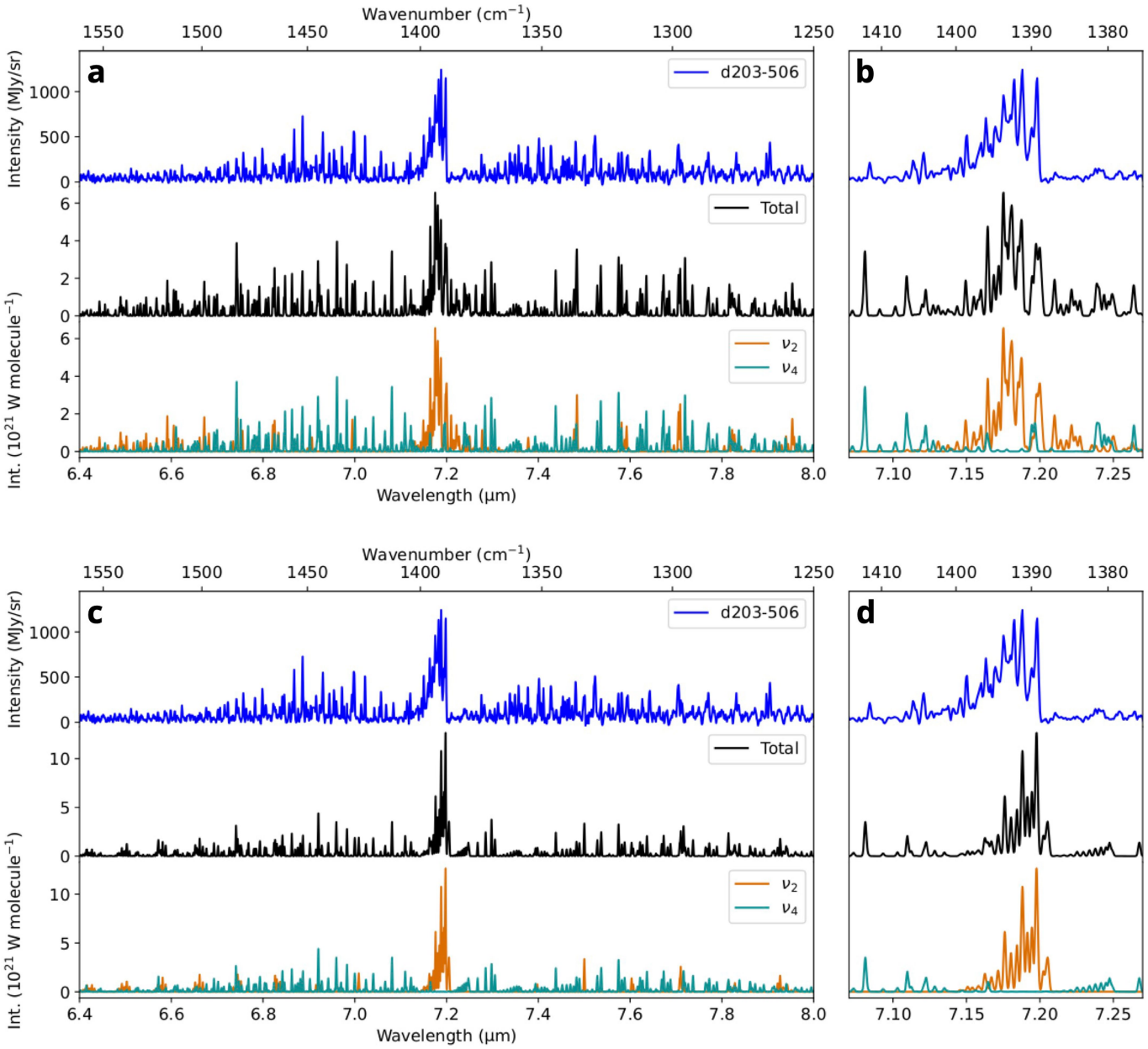

Extended Data Fig. 4 | Spectroscopic models I and II. a, Model I, with zoom on the strongest lines (**b**). **c**, Model II, with zoom on the strongest lines (**d**). For these models, the excitation temperature is $T = 400$ K, and we use a Gaussian profile of 0.35 cm^{-1} full-width-at-half-maximum.

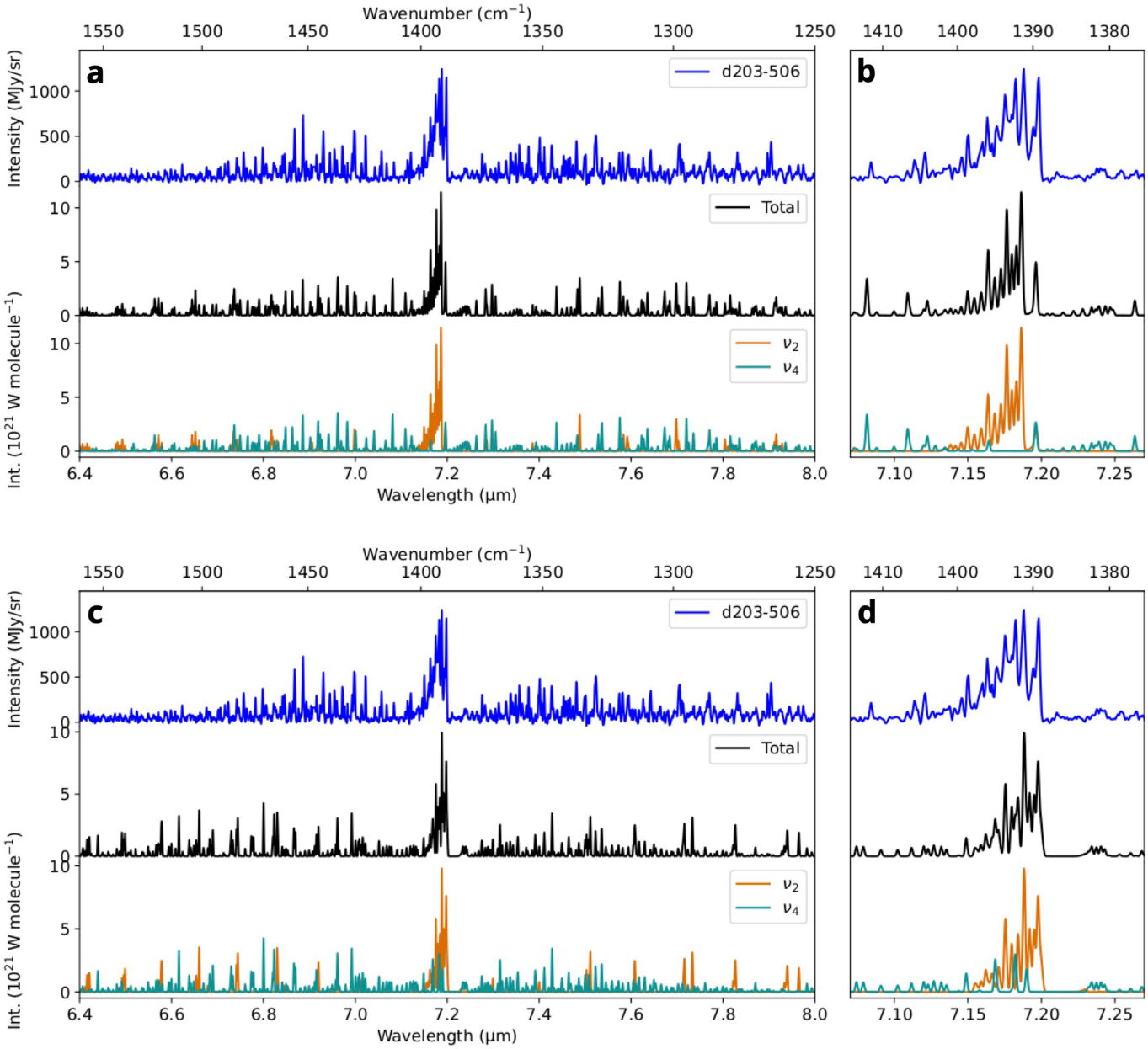

Extended Data Fig. 5 | Spectroscopic models III and IV. a, Model III, with zoom on the strongest lines (**b**). **c**, Model IV, with zoom on the strongest lines (**d**). For these models, the excitation temperature is $T = 400$ K, and we use a Gaussian profile of 0.35 cm^{-1} full-width-at-half-maximum.

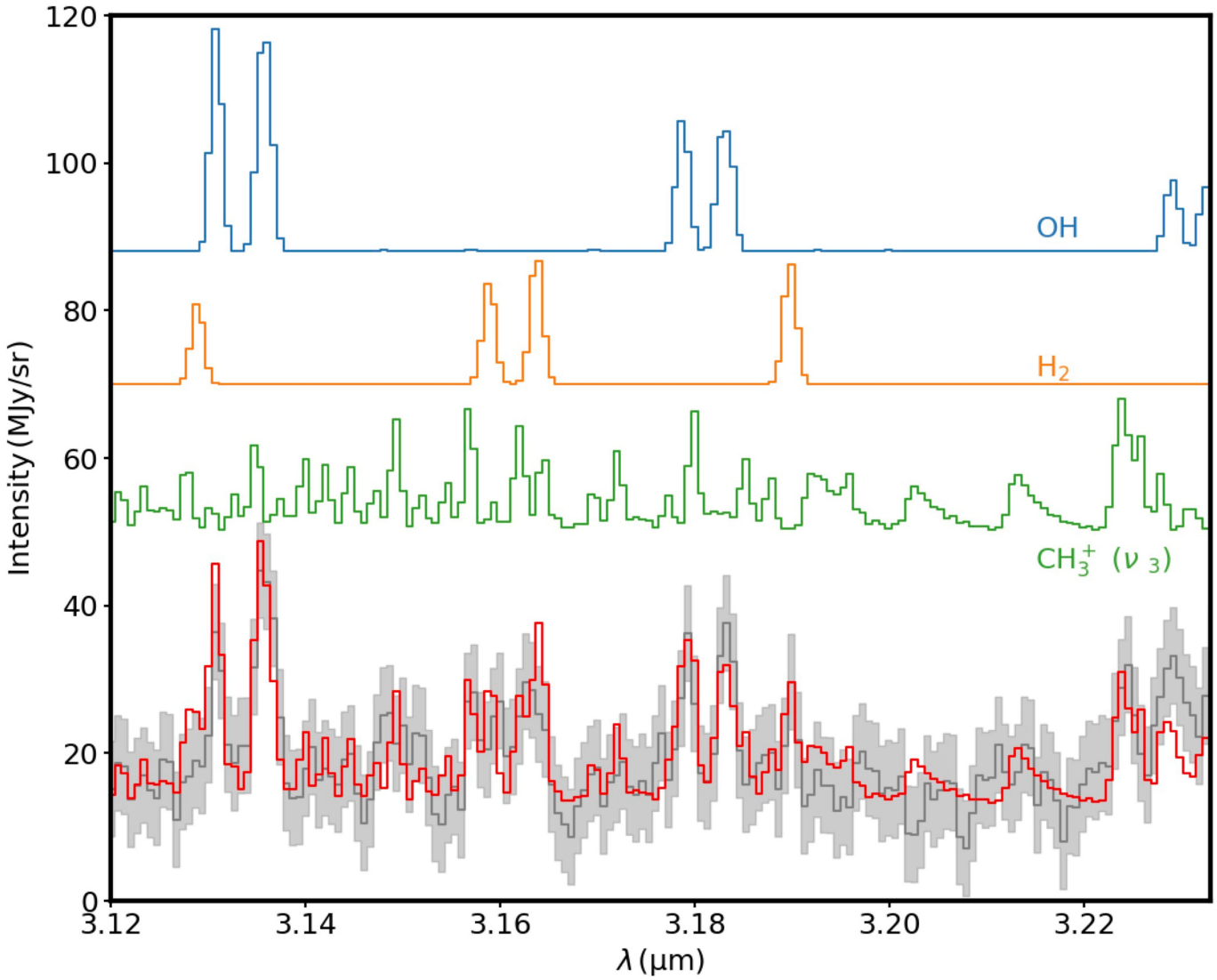

Extended Data Fig. 6 | NIRSpec spectrum of d203-506. The spectrum is shown in gray, the shaded regions is the ±3 sigma error interval of the data. This includes the error provided by the JWST pipeline, and error ν_3 band of CH_3^+ in the NIRSpec spectrum of d203-506. Model of the OH emission (blue), H_2 emission (orange), CH_3^+ emission (green), and sum of these three (red). Beyond 3.22 μm, emission due to the wings of the Aromatic Infrared Band at 3.3 μm is seen, affecting the baseline of the NIRSpec spectrum. The OH spectrum is computed with an LTE model at a temperature of 800 K. A detailed model of the OH emission will be presented in a forthcoming paper (Zannese et al. in prep). The H_2 lines are fitted individually. The CH_3^+ model used here was computed using the constants for $v = 0$ and $v_3 = 1$ from Extended Data Table 3, at 400 K.

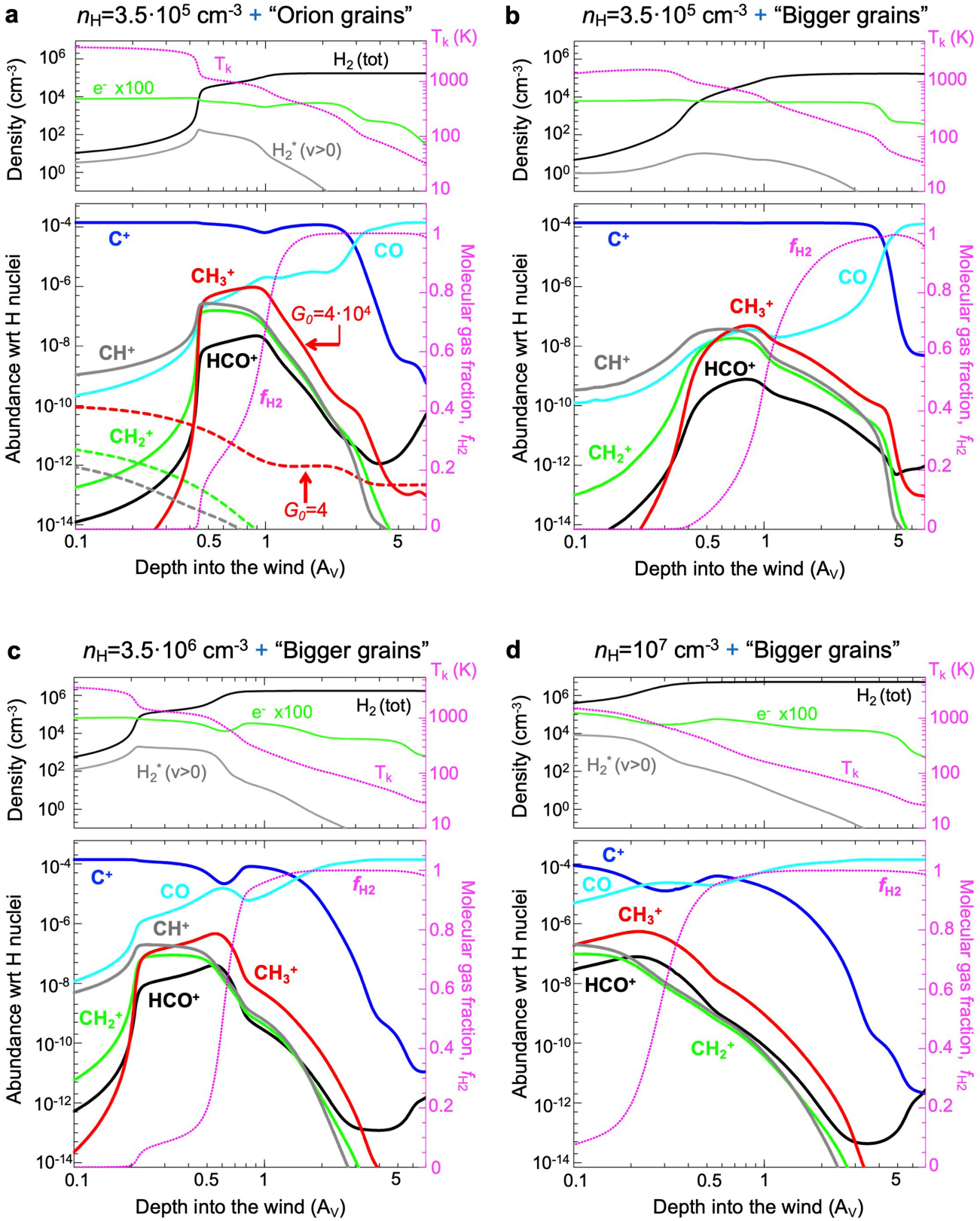

Extended Data Fig. 7 | Photochemical model results for d203-506 adopting $G_0 = 4 \times 10^4$ and different gas densities (n_H) and dust grain properties. *Upper panels*: Density and gas temperature structure as a function of visual extinction (A_V) from the wind surface. The gray curve shows the density of vibrationally excited $H_2^*(v > 0)$. *Lower panels*: Abundance profiles with respect to H nuclei. The pink dotted curves show the molecular fraction f_{H_2} profile. Dashed curves in model a) refer to a model with the same gas density but G_0 lower by a factor 10^4.

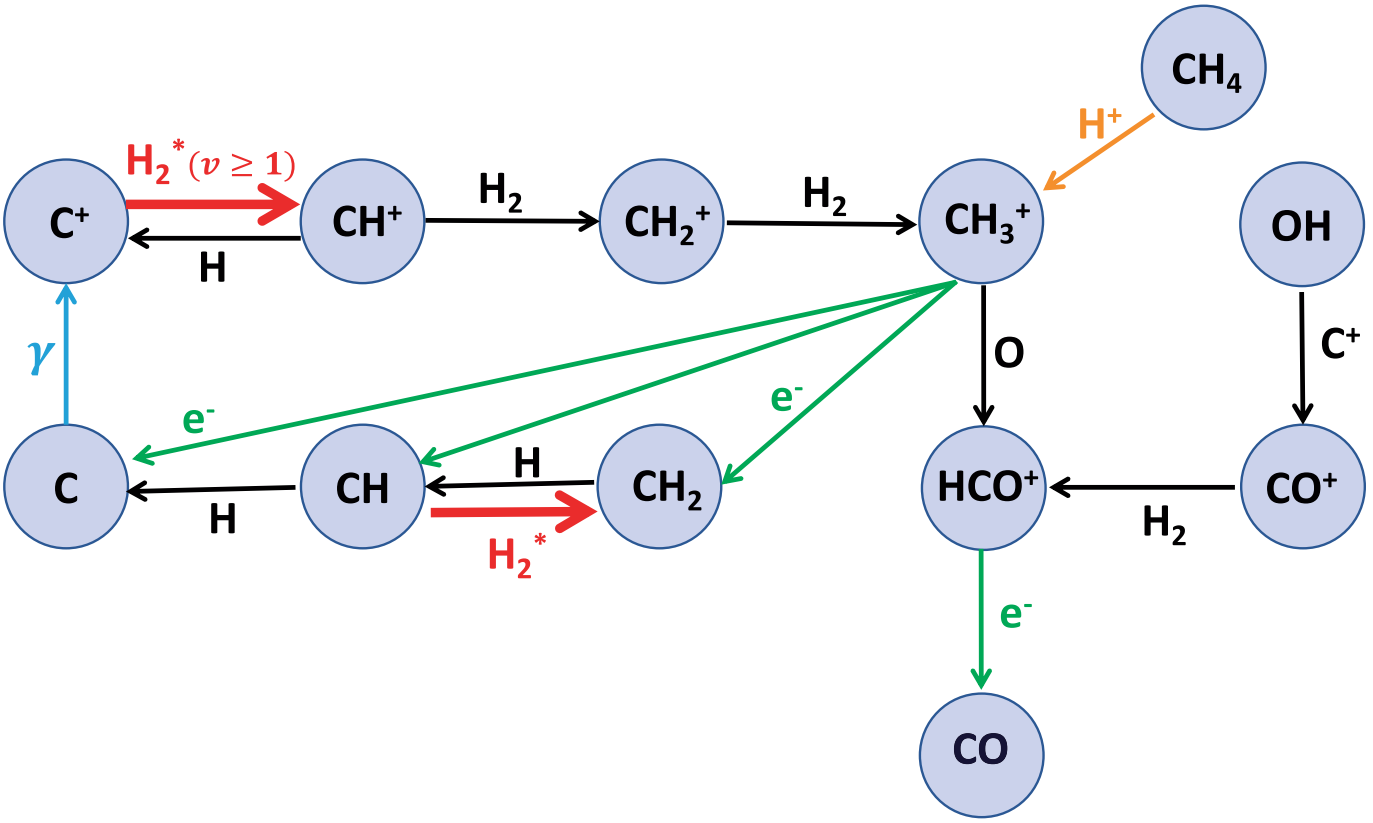

Extended Data Fig. 8 | Dominant CH_3^+ formation and destruction reactions at the CH_3^+ abundance peak predicted by the photochemical model shown in Fig. 7. This reaction network also leads to abundant HCO^+ in FUV-irradiated gas layers where $x(C^+) > x(CO)$. Red arrows show endoergic reactions when H_2 is in the ground-vibrational state $v = 0$. These reactions become fast only in disk layers where the gas temperature is high (several hundred K) and/or significant vibrationally excited H_2^* ($v \geq 0$) exists. The formation of CH_3^+ from methane will only be relevant if very high CH_4 and H^+ abundances coexist in the gas.

Extended Data Table 1 | H I detected emission lines

λ (μm) (1)	$E_{\rm up}$ (2)	A (3)	Transition (4)
5.128662	156225.1	$3.6881\ 10^{4}$	6–10
5.263685	157316.1	$1.3121\ 10^{3}$	7–18
5.379776	157257.1	$1.7812\ 10^{3}$	7–17
5.525190	157186.7	$2.4709\ 10^{3}$	7–16
5.711464	157101.8	$3.51558\ 10^{3}$	7–15
5.908220	155854.9	$7.0652\ 10^{4}$	6–9
6.291918	156869.4	$7.8457\ 10^{3}$	7–13
6.771993	156707.3	$1.2503\ 10^{4}$	7–12
7.45984	153419.7	$1.0254\ 10^{6}$	5–6
7.502502	155337.5	$1.5609\ 10^{5}$	6–8
7.508107	156498.9	$2.1174\ 10^{4}$	7–11
8.760068	156225.1	$3.9049\ 10^{4}$	7–10
9.392013	156869.4	$7.8037\ 10^{3}$	8–13
10.803593	157186.7	$2.2679\ 10^{3}$	9–16
12.387158	156498.9	$2.3007\ 10^{4}$	8–11
16.20909	156225.1	$4.6762\ 10^{4}$	8–10
19.06192	155337.5	$2.272\ 10^{5}$	7–8

(1) Emission line wavelength (μm); (2) upper level energy (K); (3) Einstein A coefficient; (s^{-1}) (4) Transition label.

Extended Data Table 2 | Pure rotational H_2 detected emission lines in MIRI MRS wavelength range

λ (μm) (1)	T_u (2)	ν (3)	A (4)	Transition (5)	Intensity ($\times 10^{-4}$) (6)
5.0531	8677.1	1978.977	$3.236\ 10^{-7}$	0-0 S(8)	0.864
5.5111	7196.7	1814.492	$2.001\ 10^{-7}$	0-0 S(7)	4.367
6.1085	5829.8	1637.046	$1.142\ 10^{-7}$	0-0 S(6)	2.582
6.9095	4586.1	1447.280	$5.879\ 10^{-8}$	0-0 S(5)	12.217
8.0250	3474.5	1246.099	$2.643\ 10^{-8}$	0-0 S(4)	4.193
9.6649	2503.7	1034.670	$9.836\ 10^{-9}$	0-0 S(3)	6.468
12.278	1681.6	814.424	$2.755\ 10^{-9}$	0-0 S(2)	2.408
17.034	1015.1	587.032	$4.761\ 10^{-10}$	0-0 S(1)	1.742

Wavelengths are from[32]. (1) Emission line wavelength (μm); (2) Upper level energy (K); (3) Transition energy (cm^{-1}); (4) Einstein A coefficient (s^{-1}); (5) transition label; (6) erg s^{-1} cm^{-2} sr^{-1}.

Extended Data Table 3 | Spectroscopic parameters of CH_3^+

	Experimental	Calculated*,[a]			Models*			
		This work[b]	Kraemer	Keceli	I	II	III	IV
$v=0$								
B	9.36214(28)	9.32	9.415	9.18	9.36214	9.36214	9.36214	9.36214
C	4.589949(35)	4.59	4.715	4.59	4.589949	4.589949	4.589949	4.589949
D_J	0.0007380(36)	0.00071	0.000719		0.0007380	0.0007380	0.0007380	0.0007380
D_{JK}	−0.0013144(79)	−0.00124	−0.001239		−0.0013144	−0.0013144	−0.0013144	−0.0013144
D_K	0.0004552(51)	0.00057	0.000568		0.0004552	0.0004552	0.0004552	0.0004552
$v_3=1$								
ν	3108.3556(18)	2948						
B	9.27239(25)	9.21		9.00				
C	4.550184(29)	4.46		4.50				
D_J	0.0007029(30)							
D_{JK}	−0.0012814(71)							
D_K	0.0004547(47)							
ζ	0.110551(38)	0.115						
η_J	−0.0006660(80)							
q^+	0.00971(17)							
$v_2=1$								
ν	1372 − 1412	1412	1391, 1433	1383, 1418	1392.80	1389.01	1391.22	1388.71
B		9.21 [9.27]	9.112 [9.06]	9.21 [9.49]	9.2270	9.3766	9.3721	9.3647
C		4.53 [4.61]	4.758 [4.63]	4.61 [4.66]	4.6392	4.6542	4.6560	4.6651
D_J			0.000715		0.002201	0.000798	.000703	.000703
D_{JK}			−0.001212		−0.005267	−0.00131	−.00118	−.00113
D_K			0.000547		0.002995	0.000488	.000455	.000455
$v_4=1$								
ν	1373 − 1393	1331	1399	1385, 1429	1374.56	1374.46	1374.54	1396.35
B		9.44 [9.50]	9.574 [9.52]	9.20 [9.48]	9.50	9.50	9.5000	9.5027
C		4.46 [4.55]	4.743 [4.62]	4.60 [4.65]	4.5776	4.5802	4.5714	4.7534
D_J			0.000719		0.000747	0.000938	.000703	.000703
D_{JK}			−0.001240		−0.00116	−0.00146	−.00128	−.00082
D_K			0.000569		0.000326	0.00032	.000455	.000455
ζ		0.115	0.1136		0.11	0.11	0.11	0.11
η_J					−0.00063	−0.00063	−0.00063	−0.00063
q^+					0.0095	0.0095	0.0095	0.0095
$< v_2=1 \vert v_4=1 >^c$								
ζ_{24}		−0.66			−0.66	−0.66	−0.66	−0.66
$< v_i=1 \vert d_i \vert v=0 >^d$								
d_2			0.084		0.084	0.084	0.084	0.084
d_3			0.102					
d_4			0.064		0.064	0.064	0.064	0.064

*Rotational, centrifugal distortion, and Coriolis constants in the ground state, v_3=1, v_2=1, and v_4=1 (in cm^{-1}), and transition moments of the v_2 and v_4 bands. Comparison of quantum calculated values, and those used to best model the spectrum of the d203-506 source around 1400 cm^{-1}. [a]Values in brakets (in blue) are scaled according to v_3=1 results when available, to v=0 otherwise. [b]ωB97X-D/cc-pVQZ, this work. [c]Coriolis interaction parameter between v_2=1 and v_4=1, unitless. [d]Transition dipole moment of the v_i fundamental bands, in Debye.